Walk on the Low Side: LOFAR Explores the Low-frequency Radio Emission of GASP Jellyfish Galaxies

Alessandro Ignesti[1] , Benedetta Vulcani[1] , Bianca M. Poggianti[1] , Alessia Moretti[1] , Timothy Shimwell[2,3] , Andrea Botteon[3,4,5] , Reinout J. van Weeren[3] , Ian D. Roberts[3] , Jacopo Fritz[6] , Neven Tomičić[7,8] , Giorgia Peluso[1,9] , Rosita Paladino[4] , Myriam Gitti[4,5] , Ancla Müller[10] , Sean McGee[11] , and Marco Gullieuszik[1]

[1] INAF-Padova Astronomical Observatory, Vicolo dell'Osservatorio 5, I-35122 Padova, Italy; alessandro.ignesti@inaf.it
[2] ASTRON, The Netherlands Institute for Radio Astronomy, Postbus 2, 7990 AA Dwingeloo, The Netherlands
[3] Leiden Observatory, Leiden University, PO Box 9513, 2300 RA Leiden, The Netherlands
[4] INAF, Istituto di Radioastronomia di Bologna, via Piero Gobetti 101, I-40129 Bologna, Italy
[5] Dipartimento di Fisica e Astronomia, Universitá di Bologna, via Piero Gobetti 93/2, I-40129 Bologna, Italy
[6] Instituto de Radioastronomía y Astrofísica, UNAM, Campus Morelia, A.P. 3-72, C.P. 58089, Mexico
[7] Dipartimento di Fisica e Astronomia, Università di Firenze, Via G. Sansone 1, I-50019 Sesto Fiorentino, Firenze, Italy
[8] INAF—Osservatorio Astrofisico di Arcetri, Largo E. Fermi 5, I-50127 Firenze, Italy
[9] Dipartimento di Fisica e Astronomia "G. Galilei", Universit´a di Padova, Vicolo dell'Osservatorio 3, I-35122 Padova, Italy
[10] Ruhr University Bochum, Faculty of Physics and Astronomy, Astronomical Institute, Universitätsst 150, D-44801 Bochum, Germany
[11] School of Physics and Astronomy, University of Birmingham, Birmingham, B15 2TT, UK

Abstract

Jellyfish galaxies, characterized by long filaments of stripped interstellar medium extending from their disks, are the prime laboratories to study the outcomes of ram pressure stripping. At radio wavelengths, they often show unilateral emission extending beyond the stellar disk, and an excess of radio luminosity with respect to that expected from their current star formation rate. We present new 144 MHz images provided by the LOFAR Two-metre Sky Survey for a sample of six galaxies from the GASP survey. These galaxies are characterized by a high global luminosity at 144 MHz ($6-27 \times 10^{22}$ W Hz^{-1}), in excess compared to their ongoing star formation rate. The comparison of radio and Hα images smoothed with a Gaussian beam corresponding to ~10 kpc reveals a sublinear spatial correlation between the two emissions with an average slope of $k = 0.50$. In their stellar disk we measure $k = 0.77$, which is close to the radio-to-star formation linear relation. We speculate that, as a consequence of the ram pressure, in these jellyfish galaxies cosmic ray transport is more efficient than in normal galaxies. Radio tails typically have higher radio-to-Hα ratios than the disks, thus we suggest that the radio emission is boosted by electrons stripped from the disks. In all galaxies, the star formation rate has decreased by a factor $\leqslant 10$ within the last ~10^8 yr. The observed radio emission is consistent with the past star formation, so we propose that this recent decline may be the cause of their radio luminosity-to-star formation rate excess.

Unified Astronomy Thesaurus concepts: Radio astronomy (1338); Extragalactic radio sources (508); Late-type galaxies (907)

1. Introduction

Star formation plays a key role in galaxy evolution, and understanding the physical effects that impact the properties and the distribution of star formation and/or the interstellar medium (ISM) are one of the main focuses of modern, extragalactic research. Among the processes able to alter the gas content of a galaxy, and hence quench its star formation, ram pressure stripping (RPS) is considered to be the most efficient mechanism in removing the ISM from galaxies in galaxy clusters (Boselli & Gavazzi 2006; Boselli et al. 2022). The most extreme examples of galaxies undergoing strong RPS are the so-called jellyfish galaxies (Smith et al. 2010; Ebeling et al. 2014; Fumagalli et al. 2014; Poggianti et al. 2017a). In the optical/UV band, these objects show extraplanar, unilateral debris extending beyond their stellar disks, and striking tails of ionized gas. Jellyfish galaxies mostly reside in galaxy clusters and are a transitional phase between infalling star-forming spirals and quenched cluster galaxies, hence they provide a unique opportunity to understand the impact of gas removal processes on galaxy evolution. Moreover, in jellyfish galaxies we can study the physics of the interplay between stripped, cold ($<10^4$ K) ISM and the surrounding, hot (~10^7 K) intracluster medium (ICM), hence obtaining insights into the more general astrophysical case of the interplay between cold clouds and hot winds.

A number of jellyfish galaxies are also found to show extraplanar, nonthermal radio emission (e.g., Gavazzi 1978; Gavazzi & Jaffe 1986; Gavazzi et al. 1995; Gavazzi & Boselli 1999; Vollmer et al. 2013; Poggianti et al. 2019a; Chen et al. 2020; Ignesti et al. 2020; Roberts et al. 2021b, 2021a; Müller et al. 2021; Ignesti et al. 2022; Luber et al. 2022; Roberts et al. 2022). In general, radio continuum emission in spiral galaxies is composed of thermal emission from ~10^4 K plasma in HII regions produced via thermal bremsstrahlung, and the nonthermal synchrotron emission of relativistic cosmic ray electrons (CRe), which are accelerated by supernovae shocks, reaching energies of a few GeV (e.g., see Condon 1992 for a review). Given the connection between supernovae and CRe and the fact that galaxies are generally optically thin to radio wavelengths, continuum radio emission is a reliable proxy to evaluate their star formation rate (SFR) (e.g., Kennicutt & Evans 2012).

At GeV energies, CRe energy losses are dominated by synchrotron emission in galactic magnetic fields with typical

values of 10–30 μG (e.g., Beck & Krause 2005, and references therein), which results in nonthermal radio emission in the 100 MHz–10 GHz band, and Inverse Compton scattering with the galactic and stellar radiation fields (e.g., Pacholczyk 1970; Longair 2011). The CRe synchrotron lifetime, $t_{\rm syn}$, determined by the synchrotron and, in a lesser extent, by the Inverse Compton losses, can be expressed as:

$$\frac{t_{\rm syn}}{\rm Myr} \simeq 34.2 \left(\frac{\nu}{\rm GHz}\right)^{-0.5} \left(\frac{B}{10\ \mu\rm G}\right)^{-1.5} \left(1 + \frac{U_{\rm Rad}}{U_{\rm B}}\right)^{-1}, \quad (1)$$

where ν is the emission frequency, B is the magnetic field intensity, and $U_{\rm Rad}/U_{\rm B}$ is the ratio between the radiation field and magnetic field energy densities (Heesen et al. 2016). In the densest region of a galaxy additional losses can also occur via bremsstrahlung and, for CRe with energies $\lesssim 1$ GeV (i.e., those responsible for the radio emission below ~200 MHz in a 10 μG magnetic field), via ionization captures (e.g., Murphy 2009; Basu et al. 2015). Therefore, the CRe radiative time depends on the combination of the aforementioned physical effects, and on the CR's energy, the magnetic and radiation fields intensity, and the local ISM density (for a detailed discussion, see Murphy 2009; Lacki & Thompson 2010; Basu et al. 2015). So CRe emitting at different frequencies have different radiative times, with CRe emitting in the 100–1000 MHz band being of the order of 10^{7-8} yr (e.g., Basu et al. 2015; Heesen et al. 2019). Within this timescale, CRe can move within the galaxies resulting in extended radio emission. CRe transport can take place either via diffusion along and across magnetic field lines, streaming, or advection. The dominant mechanism has been observed to vary in different galactic environments (e.g., see Heesen 2021 for a recent review). In the stellar disk, transport is generally dominated by diffusion. Outside of the stellar disk, such as in galactic radio halos, it is generally dominated by advection/streaming where, in the case of normal spiral galaxies, the CRe speed should be of the order of the Alfvén speed ($V = B/\sqrt{4\pi\rho}$, with magnetic field intensity B, and medium mass density ρ). In the case of jellyfish galaxies' tails, the CRe transport mechanism is advection by a ram pressure wind (Murphy et al. 2009; Vollmer et al. 2013). The CRe velocity should, therefore, be similar to the velocity of the stripped clouds which, depending on the galactic velocity and the distance from the disk, can be of the order of several hundreds of kilometers per second (Tonnesen & Bryan 2021). Hence the radio tail length, in the absence of CRe reacceleration/injection within the tail, should depend on the advection speed and the cooling timescale (e.g., Chen et al. 2020; Müller et al. 2021), resulting in a dependence of the radio tail's length on the observed frequency and, specifically, in longer radio tails at lower frequencies (Ignesti et al. 2022).

High-resolution observations have revealed radio-deficit regions on the leading edge of jellyfish galaxies (Murphy et al. 2009). Nevertheless, these systems, as well as spiral galaxies in clusters, have been reported to show a global excess of radio emission with respect to their current SFR when compared to similar objects outside of clusters (e.g., Gavazzi & Jaffe 1986; Niklas et al. 1995; Gavazzi & Boselli 1999; Boselli & Gavazzi 2006; Murphy et al. 2009; Vollmer et al. 2010, 2013; Chen et al. 2020; Roberts et al. 2021b). This

evidence has been generally explained as either being due to the compression, and resulting amplification, of the magnetic field frozen within the ISM during RPS (e.g., Boselli & Gavazzi 2006; Boselli et al. 2022; Farber et al. 2022), or as a consequence of the interactions between the CRe and the ICM-driven "shocklets". Recently, Ignesti et al. (2022) suggested that, instead, it could be due to a fast decline of the SFR within the CRe radiative time which can leave a population of old CRe which dominates the global, nonthermal radio emission, and naturally causes a discrepancy between the radio luminosity and the present SFR.

Observing nonthermal radio emission extending beyond their disk proves that jellyfish galaxies host large-scale, extraplanar magnetic fields. Previous works constrained such magnetic fields to around ~10–20 μG in the stellar disks and ~4–6 μG in the tails of two jellyfish galaxies (JO206 and JW100; see Müller et al. 2021; Ignesti et al. 2022). Such fields can affect the geometry of tails (e.g., Ruszkowski et al. 2014; Tonnesen & Stone 2014; Ramos-Martínez et al. 2018), as well as the evolution of the stripped gas. Indeed, simulations of cold gas clouds subjected to a hot wind found that magnetic fields can have a significant impact on the dynamics of wind–cloud interactions by suppressing fluid instabilities and, thus, extending the lifetime of the gas and the star-forming clouds in the stripped gas (e.g., Berlok & Pfrommer 2019; Cottle et al. 2020; Sparre et al. 2020). This physical scenario is similar to jellyfish galaxies moving in a hot ($kT \simeq 3$–8 keV) ICM, thus it suggests that magnetic fields could be crucial to preserving cold ($kT < 0.1$ keV), stripped ISM clouds in a hot, hostile environment by damping the thermal conduction between the two gases. These cold clouds could further cool down to temperatures that allow new star formation episodes tracked by both CO and Hα emission (e.g., Poggianti et al. 2019a; Moretti et al. 2020). The effect of the magnetic fields can potentially last for hundreds of Myr, thus permitting the stripped ISM to survive in form of cold clouds in the ICM (e.g., Ge et al. 2021).

The scale length of jellyfish galaxies' magnetic fields is also thought to be increased by their interaction with the ICM. A galaxy moving in a magnetized medium, such as the ICM (e.g., Carilli & Taylor 2002), can sweep up the surrounding magnetic field. This process, which is known as "magnetic draping" (e.g., Dursi & Pfrommer 2008; Pfrommer & Dursi 2010) can produce a magnetic sheath that surrounds the ISM and extends into the galaxy's wake along the tail of the jellyfish galaxy. In this scenario, as a consequence of the injection of relativistic electrons by supernovae into an ordered magnetic field, jellyfish tails should show, in the absence of depolarization effects, highly polarized synchrotron emission (Sparre et al. 2020). Indeed, deep Very Large Array (VLA) observations recently provided the first detection of these aligned magnetic fields in the tail of the jellyfish galaxy JO206 (Müller et al. 2021).

In this work we explore the nonthermal side of jellyfish galaxies by analysing the low-frequency radio emission of a subsample of objects from the GASP survey (GAs Stripping Phenomena in galaxies with MUSE;[12] Poggianti et al. 2017a). The GASP sample consists of 114 galaxies in different environments and is characterized by a range of stellar masses from 10^9 to 3.2×10^{11} $M_\odot$ with redshifts of $0.04 < z < 0.07$. The GASP project aims to investigate the process of gas

---

[12] https://web.oapd.inaf.it/gasp/

Table 1
Properties of the GASP-LOFAR Sample

Galaxy	z	$\log M_*$ ($M_\odot$)	Cluster	$z_{cluster}$	Beam (arcsec^2)	rms (μJy beam^{-1})	S_{Rad} (mJy)	L_{Rad} (10^{22} W Hz^{-1})	SFR ($M_\odot$ yr^{-1})
JW39	0.0663	11.21	A1668	0.0634	10.7×6.6	183	19.2 ± 3.2	22.8 ± 3.8	3.6 ± 0.7
J085	0.0355	10.67	A2589	0.0422	11.5×5.2	109	56.4 ± 9.6	27.0 ± 4.6	6.0 ± 1.0
JO60	0.0622	10.40	A1991	0.0586	10.8×5.5	145	14.7 ± 2.2	12.0 ± 1.8	4.5 ± 0.9
JW100	0.0619	11.47	A2626	0.0551	8.8×6.4	94	13.8 ± 2.0	10.2 ± 1.5	4.0 ± 0.8
JO49	0.0451	10.68	A168	0.0452	13.3×6.0	299	10.7 ± 2.3	5.6 ± 1.2	1.4 ± 0.3
JO206	0.0511	9.52	IIZW108	0.0489	11.9×5.4	298	18.8 ± 3.7	10.6 ± 2.3	5.0 ± 1.0

Note. From left to right: GASP name; galaxy redshift; stellar mass from Vulcani et al. (2018); host cluster name and redshift (Gullieuszik et al. 2020); resolution and rms of the 144 MHz images reported in Figure 1; integrated radio flux density and luminosity at 144 MHz; and the total SFR from Vulcani et al. (2018). The integrated radio flux densities were measured within the last contour reported in Figure 1. We report, from top to bottom, an alternative name for each galaxy: IC 4141, UGC 12582, 2MASX J14535156+1839064, IC 5337, 2MASX J01144386+0017100, and WINGS J211347.41+022834.9 (source http://cdsportal.u-strasbg.fr/).

removal in cluster galaxies by means of multiwavelength studies. In this context, low-frequency (<200 MHz) observations represent an unique probe. On one hand, at these frequencies the radio emission is usually dominated by a nonthermal component (e.g., Condon 1992; Tabatabaei et al. 2016). Hence low-frequency observations are a solid proxy of star formation (e.g., Gürkan et al. 2018; Heesen et al. 2019). On the other hand, low-frequency (∼100 MHz) observations probe low-energy particles that, due to their lower emissivity, have typical lifetimes of a factor ∼3 longer than the high-energy particles traced by high-frequency (>1 GHz) radio emission (e.g., Pacholczyk 1970). This entails that low-frequency observations probe the oldest electrons moving along the extraplanar magnetic fields and provide us the most comprehensive view of this phenomenon. For these reasons, we studied a sample of GASP galaxies with the LOw Frequency ARray (LOFAR, van Haarlem et al. 2013), that, up to date, provides the highest sensitivity and resolution at these frequencies. Previous studies of jellyfish galaxies with LOFAR are presented by Ignesti et al. (2020), Roberts et al. (2021b, 2021a, 2022), and Ignesti et al. (2022). In the latter, a multifrequency analysis of the GASP galaxy JW100 unveiled a connection between the star formation history and the nonthermal synchrotron emission.

We pursue these studies by extending them to a sample of six GASP galaxies in the northern sky. We present new LOFAR data and a series of diagnostic diagrams that we designed to characterize the local connection between the radio emission, the SFR, and the properties of the stripped gas. In this paper we use a Chabrier (2003) initial mass function (IMF) and the standard concordance cosmology parameters $H_0 = 70$ km s^{-1} Mpc^{-1}, $\Omega_M = 0.3$, and $\Omega_\Lambda = 0.7$. At the galaxies redshifts this results in $1'' \simeq 0.9$–1.1 kpc. We define the synchrotron spectrum as $S \propto \nu^\alpha$, where S is the flux density at the frequency ν and α is the spectral index.

2. Data Analysis

2.1. The GASP-LOFAR Sample

We considered a subsample of six cluster galaxies from the GASP survey (Table 1). This selection was necessarily driven by the decl. of the targets. Indeed, LOFAR can effectively observe at high sensitivity only the northern sky where only 13 out of 114 GASP galaxies are located (B.M. Poggianti et al., in preparation). In this work we present six of those galaxies observed which have been observed by the LOFAR Two-metre Sky Survey (LoTSS). For two galaxies of our sample, JW100

and JO49, the LOFAR images have been already presented by Ignesti et al. (2020, 2022) and Roberts et al. (2021b), respectively.

The galaxies of the GASP-LOFAR sample are characterized by extraplanar Hα emission produced by warm filaments of stripped ISM (Poggianti et al. 2019b). We observe galaxies where the Hα emission, in projection, is mostly contained within the disk, as well as examples of truncated disks, long tails, or unwinding arms. The sample includes both galaxies at early and advanced stages of stripping. According to the SFR–stellar mass relation (Vulcani et al. 2018), half of the sample (JW100, JW39, and JO49) shows a deficiency in SFR that indicates an advanced stage of stripping. Finally, the sample also presents a high incidence of AGN with five out of six galaxies showing nuclear activity according to the Baldwin, Phillips, & Terlevich diagnostic diagrams (BPT; Baldwin et al. 1981): JW39, JO85, and JO49 (Peluso et al. 2022) host LINER-like nuclei, while JW100 and JO206 have a Seyfert nucleus (Poggianti et al. 2017b; Radovich et al. 2019).

2.2. Data Preparation

2.2.1. LOFAR

The 120–168 MHz images presented in this work are provided by LoTSS (Shimwell et al. 2017, 2019, 2022). For details on the observation strategy and calibration of the LoTSS data we refer the reader to Shimwell et al. (2022). Following the LoTSS procedure, the data sets were calibrated by using the direction-dependent calibration and imaging pipeline DDF-PIPELINE[13] v.2.2. This pipeline was developed by the LOFAR Surveys Key Science Project and it corrects for ionospheric and beam model errors in the data. The latest version of the pipeline is described by Tasse et al. (2021). The entire data processing procedure makes use of PREFACTOR (van Weeren et al. 2016; Williams et al. 2016; de Gasperin et al. 2019), KILLMS (Tasse 2014; Smirnov & Tasse 2015), and DDFACET (Tasse et al. 2018). The observations presented here have been further processed to improve the calibration in a smaller region of the LOFAR field of view containing the target of interest, employing the "extraction and self-calibration" procedure described by van Weeren et al. (2021). We then produced the final images of the galaxies at a central frequency of the observation, 144 MHz, by using WSCLEAN v2.10.1 (Offringa et al. 2014) and using ROBUST = −0.5 (Briggs 1995). The imaging was carried out on the HOTCAT

---

[13] https://github.com/mhardcastle/ddf-pipeline

cluster (Bertocco et al. 2020; Taffoni et al. 2020). The rms map noise of each map was measured in source-free regions of the sky and it is reported in Table 1.

In order to explore the low-brightness, extraplanar emission, in this work we considered the radio surface brightness above the 2× rms level, similar to Roberts et al. (2021b). Our choice is justified by the absence of large-scale artifacts at a similar level of brightness near the galaxies. This assured us that the 2× rms level structures observed extending from the galaxies in the direction of the Hα tails are not calibration or imaging artifacts. For JW100, due to its proximity with the bright Kite radio source (see Ignesti et al. 2020, 2022), to not include possible artifacts we preferred to cut the radio emission at the 3× rms level conservatively. In the following analysis of the radio emission we adopted a calibration error of 20%, according to what is done in LoTSS (Shimwell et al. 2019, 2022). In our calculations we neglect the contribution of the thermal radio emission because, at these frequencies, it corresponds to 2%–5% of the total radio emission (e.g., Tabatabaei et al. 2017; Ignesti et al. 2022) and it cannot be differentiated from nonthermal emission with these data alone.

2.2.2. MUSE

We make use of the previous results obtained by the GASP team from the Multi Unit Spectroscopic Explorer (MUSE) optical observations of the sample. The MUSE observations, data reduction, and the methods of analysis are described by Poggianti et al. (2017a). Briefly, data were reduced with the most recent available version of the MUSE pipeline and the data cubes were averaged filtered in the spatial direction with a 5×5 pixel kernel ($\sim$1 arcsec^2). Data cubes were corrected for extinction due to dust in the Milky Way, using the value estimated at the galaxy position (Schlafly & Finkbeiner 2011) and assuming the extinction law from Cardelli et al. (1989). Emission-only data cubes were obtained by subtracting the stellar-only component of each spectrum derived with our spectrophotometric code SINOPSIS (SImulatiNg OPtical Spectra wIth Stellar population models;[14] Fritz et al. 2017). This code searches for a combination of Single Stellar Population (SSP) model spectra that best fits the equivalent widths of the main lines in absorption and emission and the continuum at various wavelengths and provides spatially resolved estimates of a number of stellar population properties, such as stellar masses and star formation histories. In particular, it provides information on the average SFR in twelve age bins. These bins can be combined into larger bins in such a way that the differences between the spectral characteristics of the stellar populations are maximal (Fritz et al. 2017).

Emission-line fluxes and errors were derived using the IDL software KUBEVIZ (Fossati et al. 2016). Only spaxels with a signal-to-noise ratio S/N(Hα) > 3 were considered as reliable. Hα luminosities were corrected both for stellar absorption and for dust extinction. The latter was estimated from the Balmer decrement assuming an intrinsic value of Hα/Hβ = 2.86 and the Cardelli et al. (1989) extinction law. SFRs were computed from the dust- and absorption-corrected Hα luminosities

---

[14] https://www.irya.unam.mx/gente/j.fritz/JFhp/SINOPSIS.html

(Vulcani et al. 2018), following the Kennicutt (1998) relation:

$$\mathrm{SFR} = 4.6 \times 10^{-42} \left(\frac{L_{H\alpha}}{\mathrm{erg\ s}^{-1}} \right) M_\odot\ \mathrm{yr}^{-1}. \quad (2)$$

In order to characterize the ionization mechanism of warm gas emitting in Hα, we consider both the BPT diagnostic diagrams presented by Radovich et al. (2019), Poggianti et al. (2019b), and Peluso et al. (2022) (using the NII lines for every galaxy with the only exception of JW100, for which we use the SII lines because the nitrogen line was contaminated by a sky line).

3. Results

3.1. The New LOFAR Images

In order to investigate the connection between the stripped ISM and nonthermal radio emission, in Figure 1 we show the contours of the radio emission at 144 MHz of each galaxy (silver, filled) on top of their emission-only, dust-corrected Hα emission. In Figure 2 we present the same contours on top of the Hα maps that have been smoothed with a Gaussian beam to match the resolution of the LOFAR images. In both figures we show also the contours of the stellar disk (gold dashed, from Gullieuszik et al. 2020). The resolution and rms noise level of each image is reported in Table 1. We note that the emission to the north of JW100 (central-left panel in Figure 1) is not related to the galaxy but it is instead part of the Kite radio source (see Ignesti et al. 2020, 2022).

The new LOFAR images reveal that in the stellar disk of these galaxies, with the only exception of JO85, the radio emission is truncated with respect to the stellar emission (i.e., the radio emission is less extended than the stellar one, leaving radio-devoid regions at the outer edges of the stellar disk). In principle, this truncation may be the result of the stripping of the ISM magnetic fields and the CRe, together with the ISM, or low-frequency flux losses occurring in the high-density, star-forming regions of the disk due to the ionization captures. The former scenario should be characterized by a lack of both radio and Hα emission at the disk edges as result of the ISM stripping, whereas in the latter we should observe Hα emission without a radio counterpart and a local flattening of the radio spectral index at low frequencies due to the loss of the low-energy CRe (e.g., Lacki 2013; Basu et al. 2015; Heesen et al. 2022). In Figures 1 and 2 we observe galaxies with signatures of stripping of both the thermal and nonthermal ISM (e.g., the northern edge of JW39), whereas evidence of ionization losses have been observed at the disk edges of JW100 in the form of flat-spectrum emission between 144 MHz and 1.4 GHz (Ignesti et al. 2022). Interestingly, in JO206 we observe both truncated radio and Hα emission in the northern half of the disk, and Hα without radio emission in the southern half. This suggests that the two processes, stripping and ionization captures, can coexist.

In general, the peak of the radio emission is close to the galactic center. We evaluated the presence of radio-loud AGN by computing the radio-loudness parameter $\mathcal{R} := (L_{1.4\ \mathrm{GHz}} / \mathrm{W\ Hz}^{-1}) / (L_{H\alpha} / L_\odot)$, where $L_{1.4\ \mathrm{GHz}}$, $L_{H\alpha}$, and $L_\odot$ are the radio at 1.4 GHz, Hα, and solar luminosities, respectively (e.g., Kozieł-Wierzbowska et al. 2017). To compute $\mathcal{R}$ we use $L_{1.4\ \mathrm{GHz}}$ measured in the NRAO VLA Sky Survey (Condon et al. 1998), and $L_{H\alpha}$ estimated from the MUSE observations by selecting the spaxels classified as LINER or Seyfert in the BPT diagrams
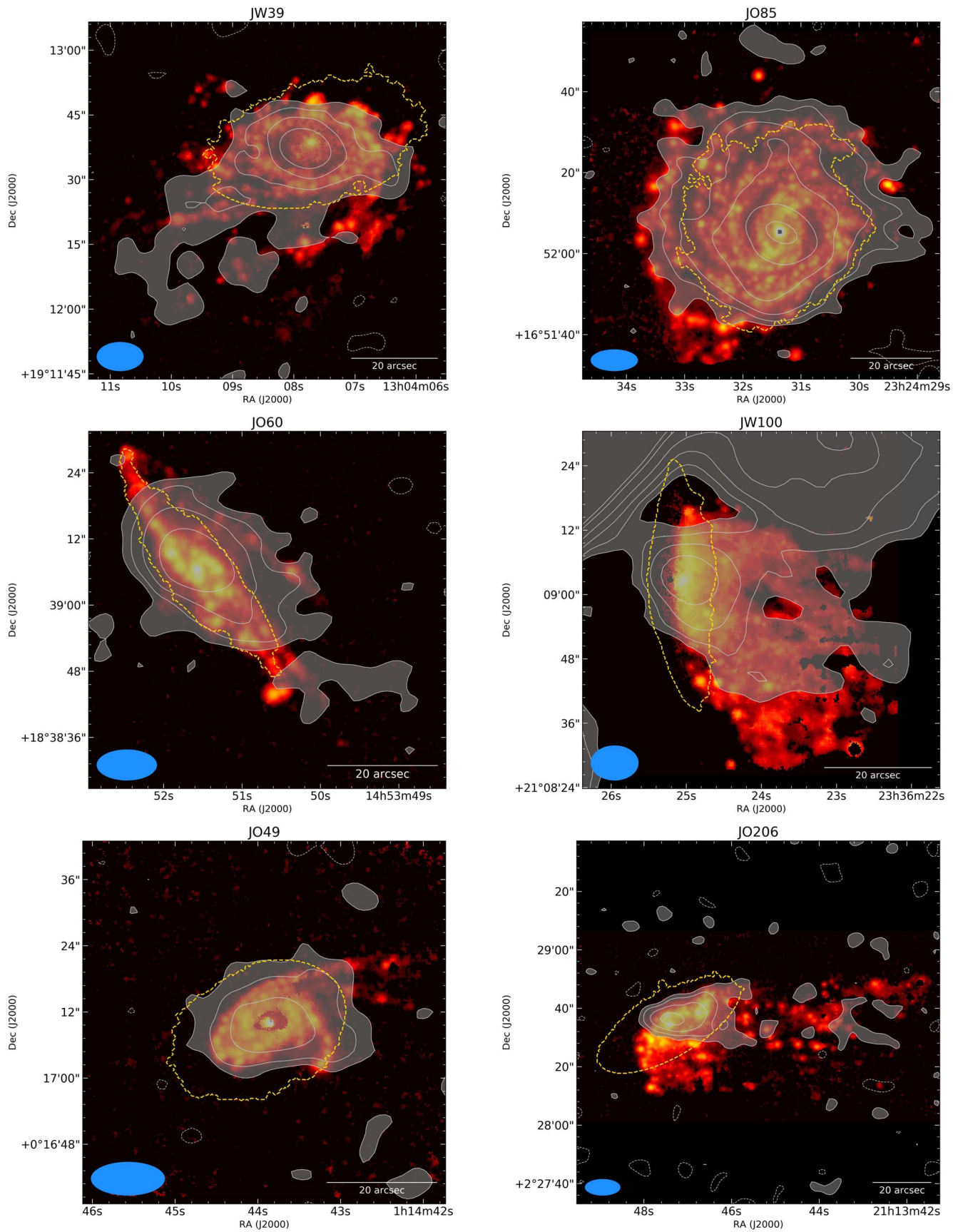
Figure 1. MUSE Hα images with the contours of the stellar continuum (gold dashed) and the LOFAR 144 MHz continuum emission (silver-filled contours). The radio continuum levels start from 2× the rms level (except JW100 for which they start from 3× the rms level) and progress by a factor 2.
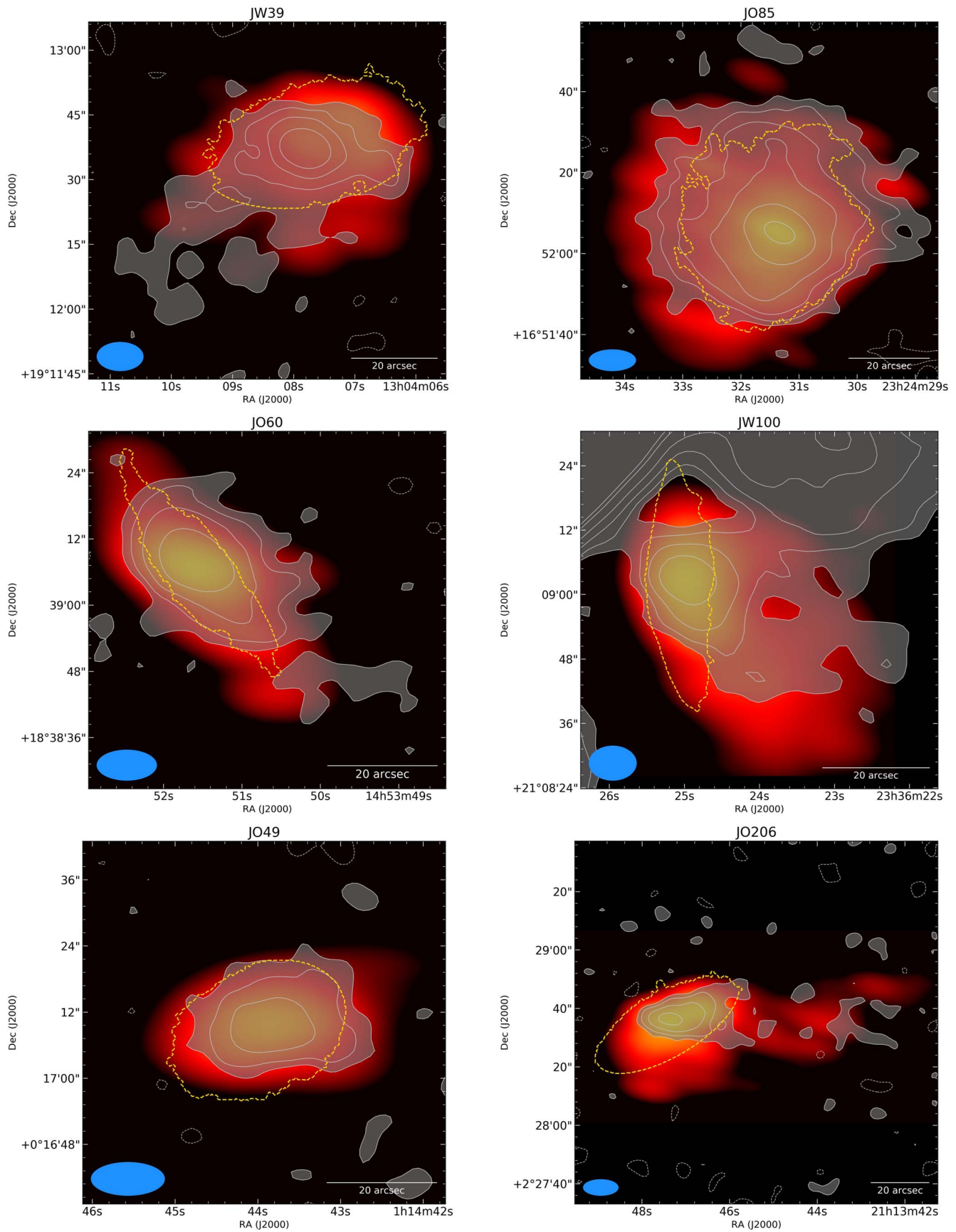
**Figure 2.** MUSE Hα images smoothed to the resolution of the corresponding LOFAR images (see Table 1) with the contours of the stellar continuum (gold dashed) and the LOFAR 144 MHz continuum emission (silver-filled contours). The radio continuum levels start from 2× the rms level (except JW100 for which they start from 3× the rms level) and progress by a factor 2.

within a circular region centered on the galactic center. A radio-loud AGN shows, typically, $\log \mathcal{R} > 15.8$, whereas in our sample we measure $13.1 < \log \mathcal{R} < 14$, thus we conclude that the GASP-LOFAR sample does not contain radio-loud AGN. Nevertheless, we cannot rule out contamination in the central emission due to low-power radio emission associated with AGN processes such as an AGN-driven wind, free–free emission from photoionized gas, low-power jets, or black hole accretion (e.g., White et al. 2017; Panessa et al. 2019).

The distribution of the radio emission with respect to the Hα emission in the stellar disks is more diverse. Figure 1 shows galaxies in which the radio and Hα emission are similarly truncated with respect to the stellar disk (JW39 and JO49), or where radio emission appears to be more truncated than Hα (JW100 and JO206), or where only radio is truncated while Hα closely follows the stellar disk (JO60). JW39, JO49, and JO206 show radio-devoid regions located on their leading edges that become more evident in the smoothed images (Figure 2). A similar feature has been observed also in the Virgo galaxies, and they have been interpreted as result of ram pressure winds stripping the gaseous ISM (Murphy et al. 2009). At odds with the other galaxies, JO85 shows no radio-devoid regions within its stellar disk, although they are present on its eastern edge. This sample shows a higher incidence of truncated disks at radio than Hα emission which might suggest that the nonthermal ISM components are more affected by the RPS than the warm plasma which, in turn, is more affected than the cold, star-forming gas because the ram pressure acceleration is inversely proportional to the gas column density (e.g., Tonnesen & Bryan 2021). We suggest that the combination of this stripping "hierarchy" and ionization captures in the high-density gas can explain the different morphologies of jellyfish galaxies at the different wavelengths, and it will be further discussed in Section 4.

JW39, JO60 and JW100 show unilateral, extraplanar radio emission extending for up to $\sim40''$ in the direction of the stripped Hα tail. JW39 shows also radio-devoid edges in the opposite direction. As observed by Murphy et al. (2009), the combination of these two features suggests that the relativistic, radio-emitting plasma could have been stripped from the disk into the tail. This provides very strong evidence that this emission is affected by the RPS. To a lesser extent, the radio emission appears to be aligned with the stripping direction in JO49. The extraplanar emission in JO206 appears to be composed of several, barely resolved patches along the stripped Hα tail, though, the detection is less certain. JO85 shows radio emission extending outside the stellar disk toward the west, which may appear at odds with the fact that it is moving southwest (Bellhouse et al. 2021).

3.2. The Radio Luminosity–SFR Relation

Cluster galaxies, and especially jellyfish galaxies, generally present an excess of radio emission with respect to their current SFR (e.g., Gavazzi & Boselli 1999; Roberts et al. 2021b). In order to test if the GASP-LOFAR galaxies follow this trend, we compare their radio luminosity at 144 MHz, including both the disk and the extraplanar emission, with their integrated SFR, measured in their disks and tails from Hα emission. The integrated flux density of each galaxy, $S_{\rm Rad}$, is evaluated within the lowest radio contour presented in Figure 1. In order to evaluate the contribution of the extraplanar radio emission, we include the emission within the contours in Figure 1 that
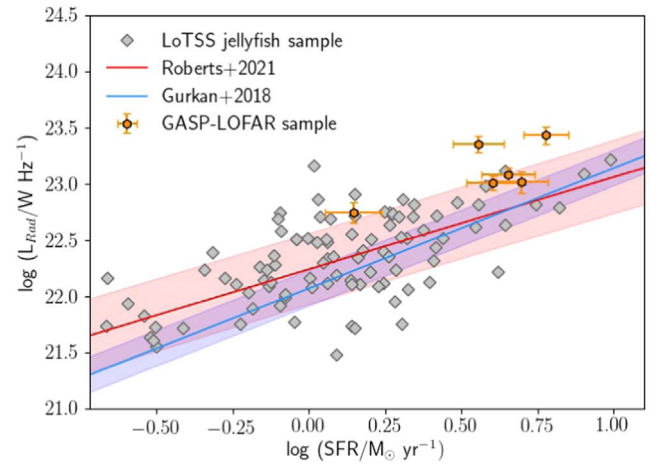
Figure 3. Radio luminosity at 144 MHz vs. SFR of the GASP-LOFAR (gold) and LoTSS (silver) samples. We report the empirical relations between $L_{\rm Rad}$ and SFR presented by Gürkan et al. (2018) (blue) and Roberts et al. (2021b) (red), the latter is fitted to the LoTSS sample. The shaded regions show the dispersion at 1σ around the corresponding best-fit relations.

coincides with the Hα tails. The corresponding error is the quadrature sum of the rms contribution in the area used for the integrated intensity measure and the calibration error. We then compute the corresponding luminosity at 144 MHz, $L_{\rm Rad} = 4\pi D_L^2 S_{\rm Rad}[(1 + z)^{\alpha-1}]$, where D_L is the luminosity distance of the hosting cluster (see Table 1).[15] The resulting radio luminosity at 144 MHz is in the range $L_{\rm Rad} = 6-27 \times 10^{22}$ W Hz^{-1}. The integrated SFRs, including disks and tails, based on the Hα emission (Table 1) are taken directly from Vulcani et al. (2018).

The values of $L_{\rm Rad}$ and the integrated SFR are reported in Table 1 and Figure 3. In the latter, we also show the values reported for 95 other LoTSS jellyfish galaxies from Roberts et al. (2021b), and the corresponding best-fitting $L_{\rm Rad}$–SFR relation at 144 MHz (red line). For reference, we show the empirical, global $L_{\rm Rad}$–SFR relation computed at 144 MHz presented by Gürkan et al. (2018) (blue line):

$$\log L_{\rm Rad} = 1.07 \pm 0.08 \times \log {\rm SFR} + 22.07 \pm 0.02, \quad (3)$$

where $L_{\rm Rad}$ and SFR are in units of W Hz^{-1} and $M_\odot$ yr^{-1}, respectively. This relation was fitted to a subsample of 15,088 star-forming galaxies with redshifts of $0 < z < 0.6$ from the seventh release of the Sloan Digital Sky Survey. The optical spectroscopic information was provided by the H-ATLAS survey (Eales et al. 2010).

The comparison with the previous studies highlights that the galaxies of the GASP-LOFAR sample generally occupy the poorly sampled high-SFR area. They show enhanced radio emission compared to the aforementioned relations (blue and red lines). They fall outside of the 1σ scatter of the Gürkan et al. (2018) relation (blue shaded area) but, with the only exception of JO85 and JW39, within the larger scatter of the LoTSS Jellyfish's relation (red shaded area). In the following, we further explore the origin of this radio excess by studying the connection between the radio and Hα emission and the SFR.

---

[15] Due to the missing information on the spectral indices of the galaxies, we prefer to neglect the k-correction. However, given the low redshift of the sample, its contribution is negligible.

3.3. Point-to-point Diagnostic Diagrams

The difference in resolution between the LOFAR and MUSE images does not permit a reliable comparison between the different maps on a pixel-by-pixel basis. Therefore, we used a point-to-point analysis[16] to compare the two emissions over larger regions. For each galaxy, we sample the radio emission with a grid composed of rectangular cells large at least as the beam of each LOFAR image (Table 1). Each cell covers a region with an average radio surface brightness above the levels discussed in Section 2.2.1. Then, we use those cells to measure simultaneously the:

1. Integrated radio flux density, $S_{\rm Rad}$, with the corresponding errors. From this quantity we derive the radio surface brightness, $I_{\rm Rad}$, (by dividing $S_{\rm Rad}$ by the area of each cell) and luminosity, $L_{\rm Rad}$, as done in Section 3.2 for the total values;
2. Integrated, dust-corrected, emission-only Hα flux density measured in the smoothed Hα maps (Figure 2). The uncertainties are defined as described in Section 2.2.2. We compute the Hα surface brightness, $I_{\rm H\alpha}$, in each cell. Then, by using only the spaxels defined as star-forming or composite in the BPT diagrams, we estimate the corresponding current SFR according to Equation (2), SFR$_{H\alpha}$; and
3. Sum of the time-averaged SFR during the last 2×10^8 (SFR$_{\rm recent}$) yr prior to observations as reconstructed with the SINOPSIS code in each spaxel (see Section 2.2.2). This time bin approximately represents the maximum radiative time of the CRe emitting at 144 MHz (e.g., Basu et al. 2015; Heesen et al. 2019).

The aforementioned quantities are combined in a series of diagnostic plots shown in Figure 4. For each galaxy, we show the sampling grid on top of the radio emission and stellar disk contours (top panel). We assign a number to each cell of the grid to ease locating the regions in the corresponding diagnostic plots. For reference, we indicate the position of the galactic center with a black cross. The diagnostic plots include the radio versus Hα surface brightness (central panel; see Section 3.3.1), and the radio luminosity versus SFR (SFR$_{\rm recent}$ and SFR$_{H\alpha}$) (bottom panel; see Section 3.3.2).

In order to test if the grids provide a reliable picture of each galaxy, we tested the total radio versus Hα surface brightness correlation with a Monte Carlo point-to-point analysis (see the Appendix), finding that the general results did not depend on the choice of the grid. This indicates that the grids are fine enough to sample the relevant spatial variations reliably (i.e., ~10 kpc at the galaxies' redshifts), and, thus, that diagnostic plots are solid. However, we are aware that the point-to-point analysis is intrinsically biased by the arbitrary choice of the sampling grid, in the sense that the position of each point on the plots necessarily depends on the geometry of the grids. For this reason, in the following we focus on the general results of the point-to-point analysis, instead of the individual features of each galaxy.

3.3.1. Radio versus Hα Surface Brightness

The comparison of the two surface brightness values can provide insights into the ISM's microphysics and the

---

[16] The point-to-point analysis was carried out with the Point-to-point TRend Extractor (PT-REX; see Ignesti 2022 for further details).

connection between the different phases responsible for the two different types of emission. In the central panels of Figure 4 we compare $I_{\rm Rad}$ and $I_{\rm H\alpha}$ computed for each cell. We identify the disk cells as those that share >10% of their surface with the stellar disk mask shown in the top panel (gold contour), and indicate them with an orange contour. In this way we can infer the differences in the $I_{\rm Rad}$–$I_{\rm H\alpha}$ spatial correlation between the total galaxy and the stellar disk only. This corresponds to analysing how the spatial correlation between the thermal and nonthermal ISM evolves from the stellar disk to the extraplanar regions. We report the errors on $I_{\rm Rad}$ and $I_{\rm H\alpha}$ derived from the respective fluxes (although the errors on $I_{\rm H\alpha}$ are almost negligible and are smaller than the marker size). In order to test the presence of possible spatial correlations, both for the total galaxy and the stellar disk only, we estimate the Spearman and Pearson correlation coefficients and fit a power law, $I_{\rm Rad} \propto I_{\rm H\alpha}^k$ (blue for the total galaxy and in orange for the disk), by using the bivariate correlated errors and intrinsic scatter method (BCES; Akritas & Bershady 1996). For reference, we plot also the global $I_{\rm Rad}$–$I_{\rm H\alpha}$ relation (green dashed line) derived by combining Equations (2) and (3), and by converting the luminosity into surface brightness:

$$\frac{I_{\rm Rad}}{\rm Jy\ arcsec^2} \simeq 5.4 \times 10^{-10} \frac{I_{\rm H\alpha}}{\rm erg\ s^{-1}\ cm^{-2}\ arcsec^{-2}}. \quad (4)$$

Equation (4) describes the global radio-to-Hα ratio expected when both emissions are powered by the total SFR. The resulting slope k, for both the total and disk-only distributions are reported in the legend of each panel, and they are summarized in Figure 5.

We find that, for every galaxy, the points lie above the global, linear correlation expected based on the standard SFR calibrations (Equation (4), dashed green line), which is expected from the global excess of radio emission of these galaxies (Figure 3). This study reveals that a sublinear spatial correlation holds between $I_{\rm Rad}$ and $I_{\rm H\alpha}$ in the form $I_{\rm Rad} \propto I_{\rm H\alpha}^k$ with an average $k = 0.50$. In the stellar disks, the average slope steepens to $k = 0.77$. The gap between the total and the disk-only slopes is more striking for those galaxies with the most evident radio tails, JW39, JO60, JW100, and JO206. Indeed in their corresponding plots we observe two distinct distributions: the disk cells which follow a steep, almost linear correlation, and those in the tail which show a flat trend with constant values of $I_{\rm Rad}$ that flatten the total slope. The implications of this result are discussed in Section 4.1. As a caveat, we note that the selection of the disk cells, and hence the resulting slope, ultimately depends on our arbitrary choice of the overlap threshold (>10%), that was chosen empirically. Due to the low number of cells used for the fit, increasing this threshold reduces the number of disk cells and, thereby, the goodness of the fit. However, the main conclusion, that is the steepening of the slopes in the disk with respect to the total, does not change.

3.3.2. Radio Luminosity versus SFR

In the bottom panels of Figure 4 we compare $L_{\rm Rad}$ with SFR$_{\rm recent}$ (gold points) and SFR$_{H\alpha}$ (red points), which trace the SFR in the last 2×10^8 and ~10^7 yr, respectively. This comparison permits us to test how much the radio excess depends on the fact that the radio and Hα emissions trace the SFR on different timescales (Kennicutt & Evans 2012). For
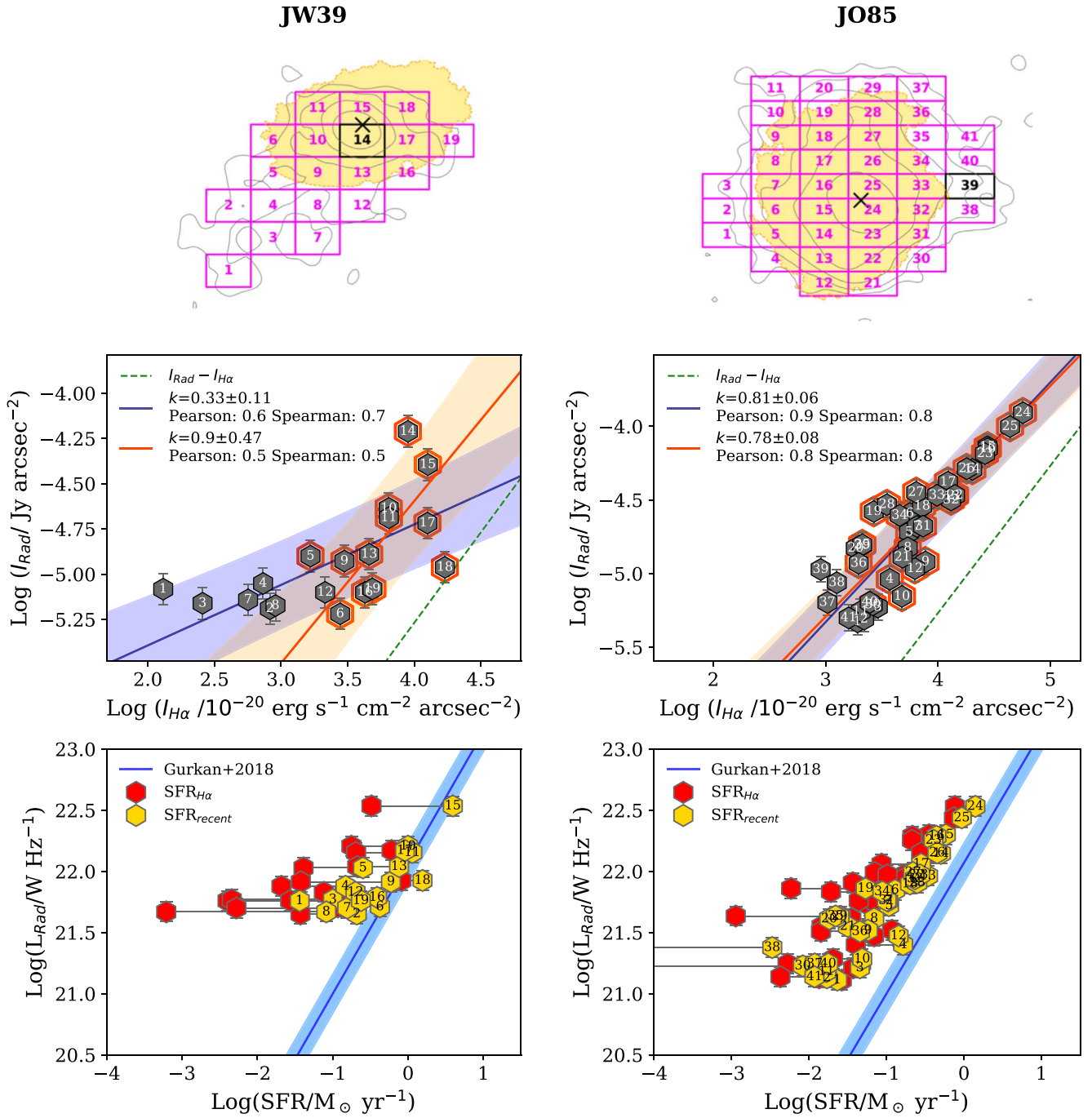
Figure 4. (a) Diagnostic plots for JW39 (left) and JO85 (right). Top: sampling grid on top of the radio (gray) and the stellar disk (orange) contours. The star-forming cells are reported in magenta. The numbers map the points in the other panels. The black crosses show the galactic center. Center: $I_{\rm Rad}$ vs. $I_{\rm H\alpha}$ measured from the maps in Figure 2 with the best-fit (continuous, blue for the total and orange for the disk-only) and the SFR-based (dashed, from Equation (4)) relations. Bottom: $L_{\rm Rad}$ vs. SFR (SFR$_{\rm recent}$, gold, and SFR$_{H\alpha}$, red), with the trend expected from Equation (3) (blue line). The shaded regions show the 1σ confidence interval of the best-fit relations. (b) Diagnostic plots for JO60 (left) and JW100 (right). (c) Diagnostic plots for JO49 (left) and JO206 (right).

reference, we show also the global trend predicted by Equation (3) (blue line). As we are interested only in the star-forming regions, we first select from the MUSE Hα emission maps only those spaxels classified as star-forming or composite in the BPT diagrams. Then we arbitrarily define as "star-forming", (magenta boxes in the top panels in Figure 4) those cells in which $\geqslant 50\%$ of the total Hα flux computed in spaxels with a BPT classification comes from those classified as star-forming and composite, and we ultimately use only the star-forming cells for this analysis.

For every galaxy, the SFR$_{H\alpha}$ points are located above the expected $L_{\rm Rad}$–SFR ratio, which is in agreement with their integrated radio luminosity excess (Figure 3). However, the SFR$_{\rm recent}$ values, which are generally higher than SFR$_{H\alpha}$, are in better agreement with the expected ratio. This is observed both in the disks and the tails, which entails that this result does not depend on the threshold adopted to select the star-forming cells. Increasing the threshold would only exclude those cells with fewer star-forming spaxels, which are usually located in the tails (Poggianti et al. 2019b). We also observe that the cells

Figure 4. (Continued.)

4. Discussion

4.1. Implications of the I_{Rad}–$I_{H\alpha}$ Spatial Correlation

The jellyfish galaxies in the GASP-LOFAR sample show sublinear I_{Rad}–$I_{H\alpha}$ spatial correlations, which are at odds with the linear, global one expected based on the standard SFR calibrators (Equation (4)). Moreover, all the points are located above this relation, which indicates that radio-to-Hα excess is
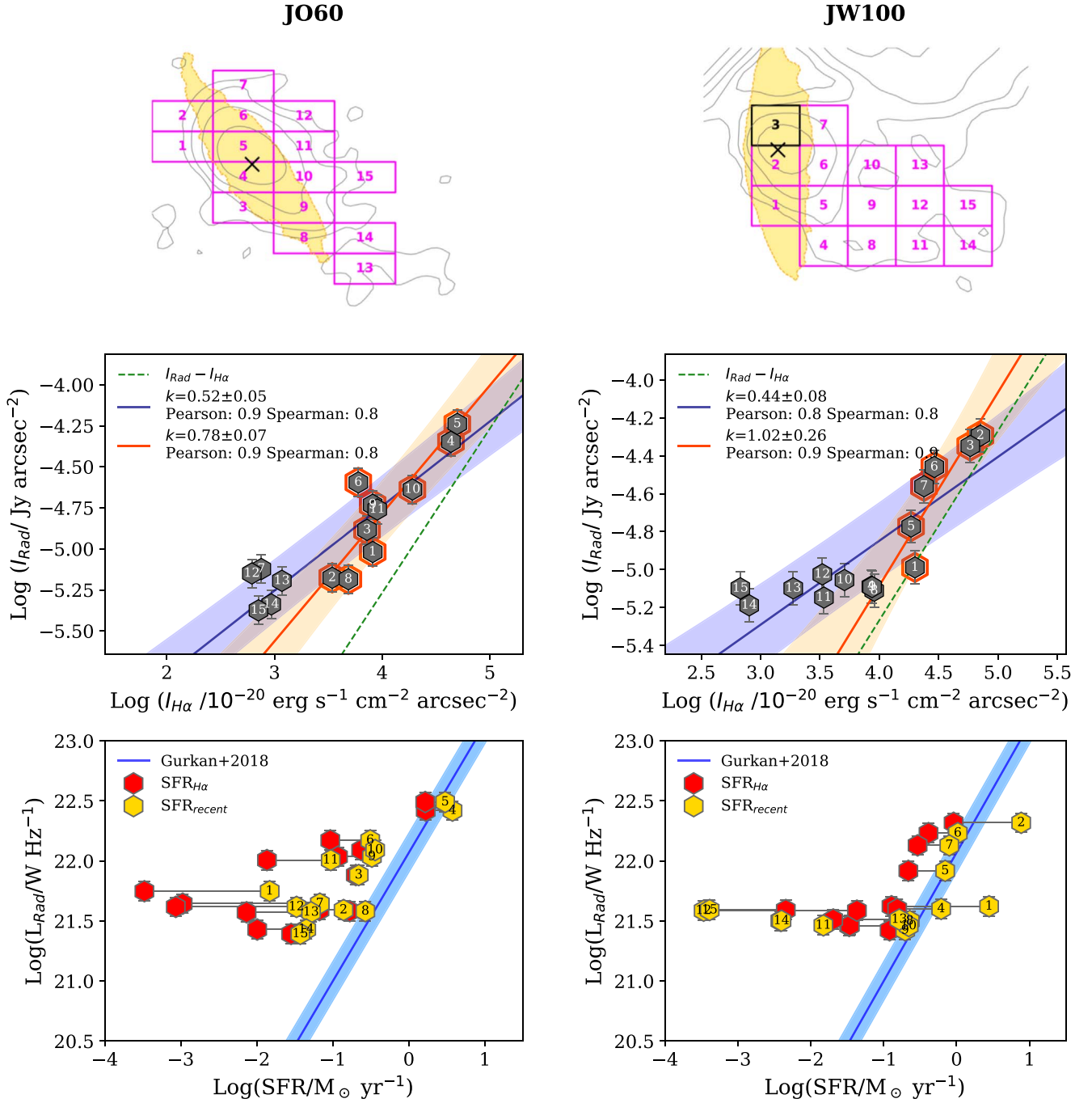
adjacent to the AGN show radio-to-SFR ratios that are in line with the rest of the galaxy, further suggesting that contamination from any AGN radio emission is limited (see Section 3.1). This result is going to be further discussed in Section 4.2.

ubiquitous in these galaxies. These results suggest that the nonthermal radio emission does not depend solely on the local, ongoing star formation. The galaxies with the most extended extraplanar emission (JW39, JO60, JW100, and JO206) show different trends in the total and disk slopes, with the slopes measured in their disks being systematically steeper than those derived by using the whole galaxy (Figure 5). Moreover, the more distant, faintest regions have, on average, a constant I_{Rad} and higher ratios of radio-to-Hα emission with respect to Equation (4) than those in the disk.

The existence of sublinear spatial correlations between the resolved nonthermal radio emission and the ISM star formation tracers in spiral galaxies has been previously reported in the

JO49

JO206
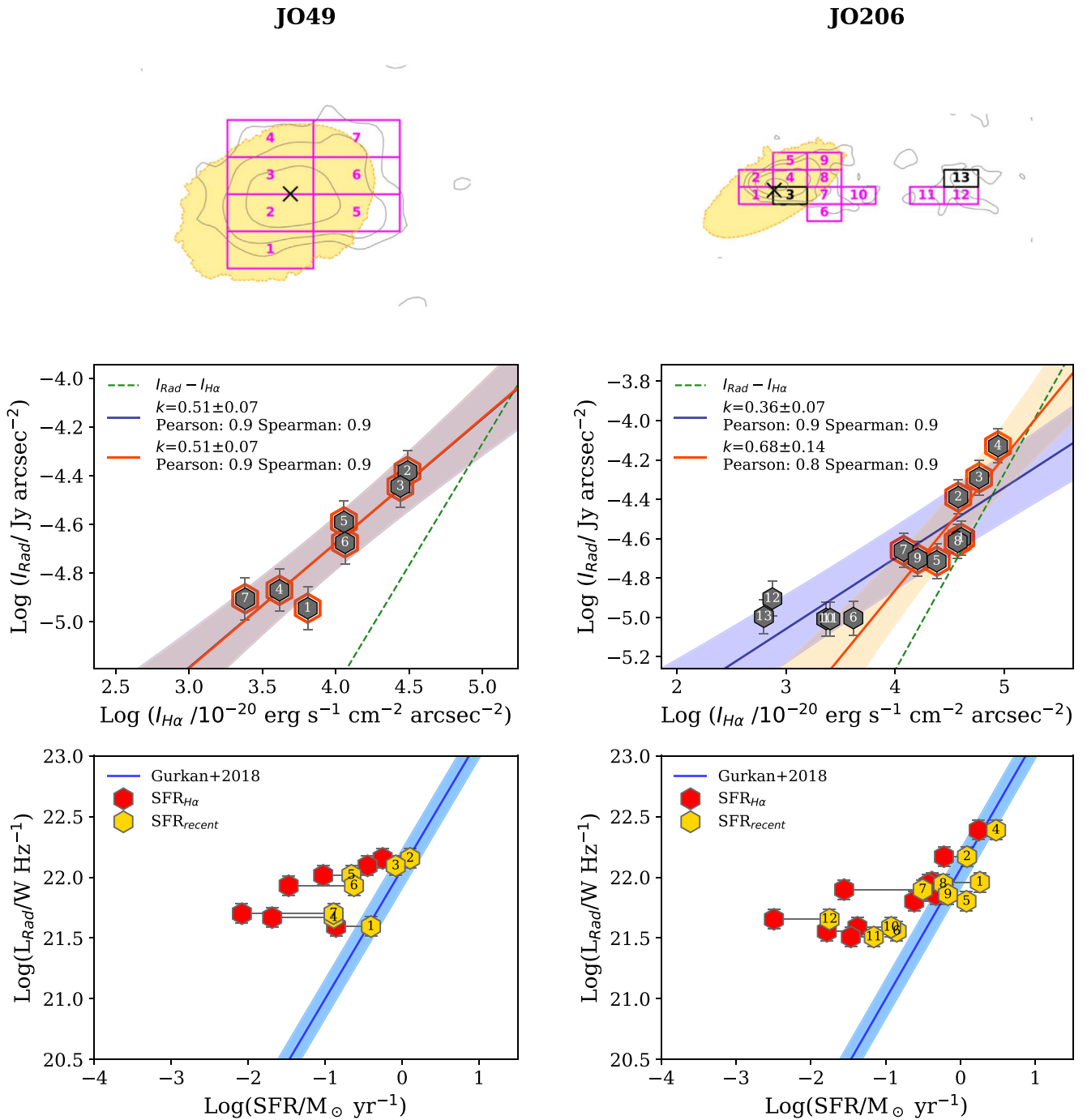
Figure 4. (Continued.)

literature (e.g., Hoernes et al. 1998; Berkhuijsen et al. 2013; Heesen et al. 2019). In general, the correlation slope can depend on the observed radio frequency, where the lower the frequency, the flatter the correlation, or on the radio spectral index, where the steeper the spectral index, the flatter the slope (Heesen et al. 2019). These pieces of evidence suggest that CRe diffusion plays a role in defining these spatial correlations and, more specifically, that the flattening of the slope is a consequence of CRe transport away from star-forming regions. This would entail that old CRe, which can be traced by low-frequency observations, should be mainly responsible for the spatial correlations flattening because they have been

transported over large scales during their radiative time. In this framework, the sublinear spatial correlations observed in the disks of the GASP-LOFAR sample (Figure 5) could be explained by a combination of radio emission dominated by the old, steep-spectrum CRe, which is consistent with the steep-spectrum nonthermal radio emission observed for JO206 and JW100 (Müller et al. 2021; Ignesti et al. 2022), and efficient CRe transport.

For JW39 and JW100 the disks' slopes are consistent with linearity, that is the trend expected from Equation (4). This may suggests that the smoothing scale (∼10 kpc) is similar to the CRe transport scale, and, hence, the slopes resemble the
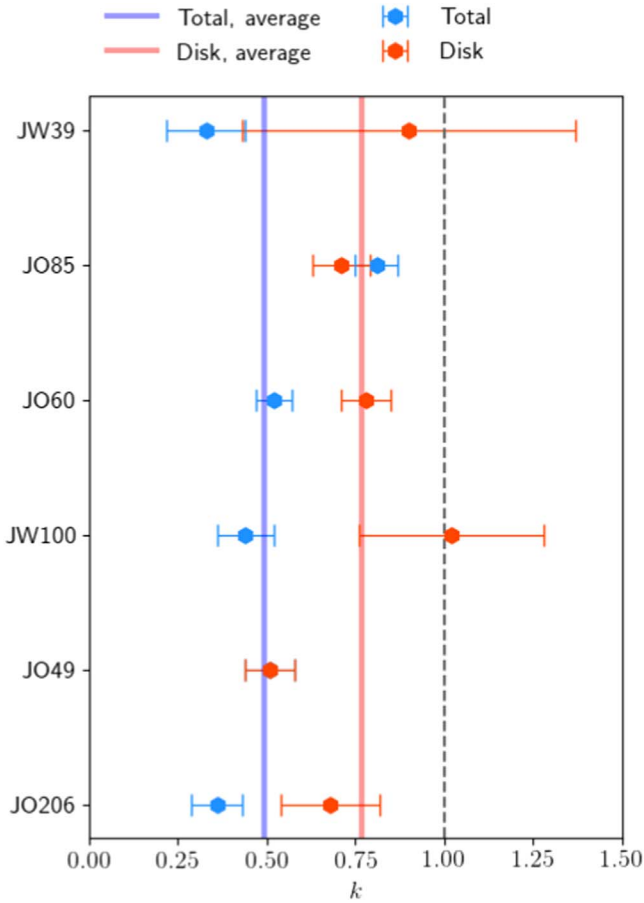
Figure 5. Slope k of the $I_{Rad}-I_{H\alpha}$ relation for each galaxy (Figure 4). The vertical lines indicate the mean value of each distribution and the $k = 1$ level (dashed gray line).

standard SFR calibrators. Therefore, the spatial correlation slopes observed in the disks of JW39 and JW100 are consistent with the idea that the CRe transport scale in these galaxies is larger than observed in spiral galaxy disks ($\sim$1–5 kpc). We investigate this result by comparing the spatial scales, L, of the two principal CRe transport processes in these systems: diffusion and advection. In the case of CRe diffusion, the spatial scale is:

$$L = \sqrt{4D\tau} \simeq 1.1 \times \sqrt{\frac{D}{10^{28} \text{ cm}^2 \text{ s}^{-1}} \frac{\tau}{10 \text{ Myr}}} \text{ kpc,} \quad (5)$$

where τ is the timescale and D is the diffusion coefficient, which depends on the CRe energy and the local magnetic field power spectrum, and can vary between 10^{27} and 10^{29} cm^2 s^{-1} (Strong et al. 2007). For advection, the typical spatial scale is:

$$L = V \cdot \tau \simeq \frac{V}{100 \text{ km s}^{-1}} \frac{\tau}{10 \text{ Myr}} \text{ kpc,} \quad (6)$$

where V is the CRe velocity. Equation (5) shows that to reach $L = 10$ kpc, for a typical $D = 1 \times 10^{28}$ cm^2 s^{-1}, the timescale is of the order of $\sim$900 Myr, which is longer than the typical CRe radiative time in galactic disks. Covering these spatial scales in $\leqslant 10^8$ yr requires a diffusion coefficient of $D \geqslant 9 \times 10^{28}$ cm^2 s^{-1}, which is slightly higher than observed in spiral galaxies (e.g., Strong et al. 2007; Tabatabaei et al. 2013; Heesen et al. 2019). On the other hand, these scales could be consistent with

the CRe advection (Equation (6)), as a typical velocity of 100 km s^{-1} would be able to cover 10 kpc in $\sim$10 Myr, which is more reasonable for low-energy electrons emitting at 144 MHz. Therefore, our results might hint that CRe transport in the disks of these jellyfish galaxies, JW39 and JW100, is either dominated by advection, due to ram pressure which is stripping the nonthermal ISM (see Section 3.1), or that the CRe diffusion might be more efficient than in normal galaxies. The diffusion coefficient D depends on the local magnetic field configuration and turbulence spectrum (Strong et al. 2007), thus it may be possible that the RPS, by affecting the ISM's microphysics, may induce higher values of D and, hence, more efficient CRe diffusion (Equation (5)) than observed in normal spiral galaxies. However, we note that, for the rest of the sample, the spatial correlations in their stellar disks are not consistent with linearity (Figure 5). We argue that this might be due to projection effects that mix the disk and the extraplanar emissions, which, on the basis of what we observe for JW39, JO60, JW100, and JO206, follows a flat, almost uniform, distribution. Thus this blend may result in a flattening of the disks' slopes. Another possible explanation could be a discrepancy between the sampling resolution and the transport scale that was not solved by the smoothing.

Concerning the extraplanar emission, observing a sublinear $I_{Rad}-I_{H\alpha}$ relation might shed some light on the physics of the stripped ISM. Previous studies reported that jellyfish galaxies commonly show a steepening of the radio spectral index in extraplanar emission (Vollmer et al. 2004; Müller et al. 2021; Ignesti et al. 2022; Roberts et al. 2022) that indicates that the CRe in these regions were originally accelerated in the disk and subsequently swept in the tail by ram pressure winds. In the case of the radio tails observed in the GASP-LOFAR sample, which show projected lengths of $\sim$40 kpc, Equation (6) indicates that a ram pressure wind speed of $V \geqslant 400$ km s^{-1} would be required to transport the CRe in $\leqslant 10^8$ yr. For comparison, for magnetic field intensities of $B \leqslant 10$ μG (Ignesti et al. 2022), and CRe energy losses dominated by synchrotron radiation (i.e., $U_{Rad}/U_B \simeq 0$), Equation (1) yields $t_{syn} \geqslant 9 \times 10^7$ yr for CRe emitting at 144 MHz in the tails. Concerning the wind speed, albeit the total velocity of these galaxies is still unknown, the line-of-sight velocities for JW39, JO60, JW100, and JO206 are 820, 1000, 1950, and 632 km s^{-1}, respectively (Gullieuszik et al. 2020). Therefore, the observed radio tails lengths are consistent with a pure advection scenario. Our results provide complementary pieces of evidence for this scenario. Observing that the extraplanar regions, located farthest from the trend defined by Equation (4), can be naturally explained by the presence of additional electrons coming from the disk that flatten the spatial correlation slope by boosting the local radio emission in the extraplanar regions with the faintest Hα emission.

4.2. Echoes of Past Star Formation

The GASP-LOFAR galaxies, analogously to cluster galaxies, show an excess of radio emission with respect to the ongoing SFR (Figure 3). As highlighted by the L_{Rad}–SFR plots (Section 3.3.2), this excess does not appear to be localized on the leading edges of the galaxies (as observed by Murphy et al. 2009), but it is ubiquitous over the galaxies. Historically, this radio excess has been explained as the result of ISM
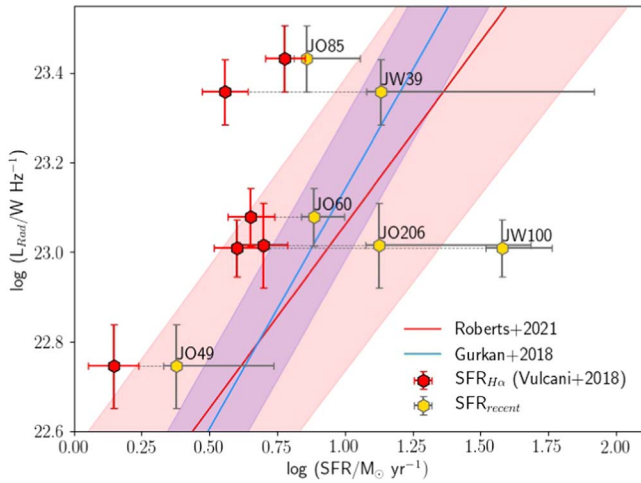
Figure 6. Integrated radio luminosity at 144 MHz vs. SFR. For each galaxy, the $SFR_{H\alpha}$ from Vulcani et al. (2018) (red points) and SFR_{recent} (gold points; see Section 3.3), with the corresponding errors, are connected by the dashed lines. We show also the best-fit L_{Rad}−SFR relations from Gürkan et al. (2018) (blue line) and Roberts et al. (2021b) (red line). The shaded regions show the dispersion at 1σ around the corresponding best-fit relations.

compression, or due to the contribution of CRe reaccelerated by ICM winds (e.g., Gavazzi et al. 1995; Boselli & Gavazzi 2006; Murphy et al. 2009). In Ignesti et al. (2022) we presented an alternative view based on a multifrequency analysis of JW100. By comparing the excess of SFR between the radio and Hα estimates with the average SFR inferred by the stellar population synthesis, we found the radio excess in its stellar disk to be consistent with a decline of the SFR happening within the timescale of the radio emission (i.e., 10^{7-8} yr). This scenario was further supported by the fact that the nonthermal emission in both the disk and the tail of JW100 showed evidence of spectral steepening above 1.4 GHz, thus indicating that the radio emission is dominated by old CRe.

In this work we further explore the hypothesis of a connection between the radio luminosity excess and the SFR decline. In the L_{Rad} versus SFR point-to-point plots (Section 3.3.2) we observe that SFR_{recent}, which is generally higher than $SFR_{H\alpha}$, is close to the expected ratio (blue line in Figure 4, bottom plots), especially for the central regions. In the extraplanar regions the excess seems to persist, which would be consistent with the idea of a local radio emission boost provided by the CRe advected from the disk by ram pressure winds. In Figure 6 we present the integrated L_{Rad} and $SFR_{H\alpha}$ for the GASP sample (red points; see Table 1) and the corresponding integrated SFR_{recent} (gold points). For every galaxy $SFR_{recent} > SFR_{H\alpha}$, which indicates that the SFR in these galaxies declined in the last 2×10^8 yr. The extent of the SFR decline varies within the sample, ranging from a factor ~ 10 in JW100 to ~ 2 in JO85.

Overall, we observe that SFR_{recent} is in better agreement than $SFR_{H\alpha}$ with the global, empirical relations (blue and red lines; from Gürkan et al. 2018; Roberts et al. 2021b). Specifically, we measure a decrease of the rms deviations from 0.5 to 0.4 and from 0.4 to 0.3 for the Gürkan et al. (2018) and Roberts et al. (2021b) relations, respectively, as more galaxies are fit within the 1σ scatter (Figure 6). At odds with the other galaxies, the total radio emission of JW100 appears to be more in agreement with the current SFR rather than the past one, whereas in the

stellar disk the radio emission is well explained by the past star formation (Ignesti et al. 2022).

The results shown in Figure 6 support the idea that the current radio emission is related to the past, higher SFR, (or, in other words, that the radio emission is dominated by old CRe) and thus, that the jellyfish galaxies' radio excess is a consequence of the fast evolution of the star formation activity induced by the RPS in these galaxies. Qualitatively, a past phase of higher SFR would entail a higher CRe injection, thus a higher radio emission. When the SFR declines, the CRe injection should decline correspondingly. But if the decline timescale is fast ($\sim 10^7$ yr) , such as in the case of those galaxies heavily processed by RPS, and shorter than the CRe radiative time, its effect on the total radio emission (especially at lower frequencies) goes unseen because the bulk of the radio emission is produced by the old CRe injected previously. On the contrary, tracers which probe the most recent SFR (e.g., Hα) are affected by the SFR decline (e.g., see Cleland & McGee 2021 for a study of the SFR evolution with multiple tracers). Thus the result is that the radio emission appears in excess with respect to the current SFR.

Observations at higher frequencies will be able to test this scenario conclusively. Observing signatures of a old, steep-spectrum CRe population (i.e., spectral steepening at frequencies above 1 GHz) would confirm that the radio emission is dominated by the older CRe injected during a past phase of higher SFR. Indeed, evidence of steep-spectrum emission at high frequencies has already been reported for JW100, which shows an integrated, nonthermal spectral index of $\alpha = -0.92 \pm 0.15$ and -2.43 ± 0.37 in the 1.4–3.2 and 3.2–5.5 GHz bands, respectively, in the disk, and $\alpha < -0.85$ between 1.4 and 3.2 GHz in the tail (Ignesti et al. 2022); and for JO206, which shows $\alpha \simeq -1$ in the disk and $\alpha \simeq -2$ in the tail between 1.4 and 2.7 GHz (Müller et al. 2021). Moreover, by comparing the detection levels of JO206's radio tail in the new LOFAR data and in the maps presented by Müller et al. (2021), we can now roughly constrain the spectral index between 144 MHz and 2.7 GHz to $\alpha = -1.1$, which further indicates that the synchrotron spectrum is curved, i.e., that the CRe population is old. In order to test this scenario conclusively, a study of the spectral indices in the GASP-LOFAR sample will be the object of future work. This scenario should also imply that the radio excess broadly depends on the observed radio frequency. Observations at higher frequencies trace CRe with higher energies and shorter radiative times, hence more similar to the other tracers and more sensible to the SFR decline. On the contrary, observations at lower frequencies, such as the ones that are going to be provided by the LOFAR LBA Sky Survey (de Gasperin et al. 2021), should observe a higher radio excess because they trace CRe with longer radiative times. This scenario can be further explored also by detailed numerical simulations of these galaxies to trace CRe evolution by taking into account the different transport process and the different energy loss mechanisms in a multiphase ISM.

Our conclusions do not rule out that the other processes proposed previously in literature (such as magnetic field amplification due to ISM compression or CRe reacceleration; see Section 1) that could further contribute to producing the jellyfish galaxies' radio luminosity excess. However, we note that the results in Figure 4 challenge the scenario of radio excess due to ISM compression (Boselli & Gavazzi 2006). In the I_{Rad} versus $I_{H\alpha}$ plots we observe that

the radio excess is not limited to the regions in the compressed zone (i.e., where the contours of the radio emission are more dense) and, on the contrary, in some cases we observe that these regions, which should be the most compressed by RPS, are the closest to the expected radio–Hα ratio. This could result from multiple effects in action. It could be that in those regions, due to the increased density of the compressed ISM, low-energy electrons emitting at 144 MHz are more affected by ionization capture (e.g., Basu et al. 2015), thus balancing the synchrotron emissivity enhancement due to RPS. It could be that those regions, as a consequence of ISM compression, are harboring an intense phase of ongoing star formation that dominates the local radio emission and, therefore, they are less affected by the echoes of past star formation. Furthermore, we note that, due to the radio images' resolution, the sampling cells located on the leading edges of some of these galaxies include both radio-rich and -deficient star-forming regions (Figure 2). This blend may result into a seemingly regular radio-to-SFR ratio.

5. Summary and Conclusions

We presented a study of the extended, nonthermal radio emission at 144 MHz for a sample of six jellyfish galaxies from the GASP sample. The GASP-LOFAR sample shows high radio luminosities ($6-27 \times 10^{22}$ W Hz^{-1}), and a series of recurring patterns in the radio and Hα morphologies, such as truncated radio emission with respect to the stellar disk and extraplanar components. These results highlight that nonthermal ISM components, i.e., CRe and magnetic fields, are heavily influenced by the RPS, similar to the warm, ionized ISM. We observe an excess of radio luminosity in the GASP-LOFAR sample with respect to their current SFRs. This is in agreement with the previous studies of jellyfish galaxies, and cluster galaxies in general. We devise a series of diagnostic plots to frame the connection between ISM stripping, star formation history, and radio emission. We found that a sublinear relations hold between the radio and Hα surface brightnesses ($I_{\mathrm{Rad}} \propto I_{\mathrm{H}\alpha}^k$) with an average slope of $k = 0.50$, whereas in the stellar disks we measure $k = 0.77$. The extraplanar regions have, in general, a higher relative deviance from the expected radio luminosity–SFR relation than those in the disk. We argue that this is due to the presence of CRe coming from the disk that boost the local radio emission.

We observe that for JW39 and JW100 the $I_{\mathrm{Rad}}-I_{\mathrm{H}\alpha}$ correlation in their stellar disks is consistent with being linear, which would agree with the trend expected from the SFR calibrators. We speculate that it is because the smoothing scale is consistent with the CRe transport scale. In this case, a spatial scale of ∼10 kpc would entail that the CRe transport in their stellar disks is more efficient than observed in normal spiral galaxies. We speculate that this large spatial scale could be explained either by CRe transport dominated by advection rather than diffusion, or a diffusion efficiency higher than usual induced by RPS.

From the comparison between the radio luminosity and the recent SFR evolution, both local and integrated, it emerges that the SFR of these galaxies declined in the last 10^8 yr, and that the radio luminosity can be explained better by the past, higher SFR than by the ongoing one traced by the Hα emission. The implications are twofold. On the one hand, our work shows that combined radio–Hα studies can constrain the SFR history. On the other hand, the radio luminosity excess could emerge when the timescale of the SFR decline is shorter than the CRe radiative time, leaving a population of old CRe that produces the bulk of the radio emission. CRe advection by ram pressure outside of the disk would then be responsible for the extraplanar radio emission. This connection between star formation history and radio luminosity might hint that, in general, the integrated radio luminosity excess of cluster galaxies could be a signature of a (fast) SFR decline. This work is among the few studies comparing the resolved properties of Hα and low-frequency radio emission, and is surely focused on a peculiar class of objects. However, the intimate connection between the recent, instead of the ongoing, star formation and the radio emission could be a general property of cluster galaxies that have similar star formation histories. Future studies on larger samples of galaxies, including those not evidently affected by ram pressure, will help clarifying the possible caveats in using low-frequency radio emission as a tracer for ongoing SFR.

The results presented here call now for follow-up observations at higher frequencies. By combining these new pieces of information with detailed spectral index maps it will be possible to study the CRe lifecycle within these galaxies. Moreover, our findings provide a benchmark for numerical simulations of RPS, or more in general of cloud-crushing scenarios. The fact that, thanks to LOFAR, we are discovering more and more jellyfish galaxies with extraplanar, nonthermal radio emission indicates that large-scale magnetic fields are common in these systems, and that their evolution is intimately connected with the evolution of the stripped gas.

Appendix
Monte Carlo Point-to-point Analysis

We tested the reliability of the grids adopted in the point-to-point analysis (Figure 4) by performing a Monte Carlo point-to-point analysis (MCptp; for further details see Ignesti 2022). For each galaxy, we obtained 100 different samples of the radio emission with randomly generated grids (each grid with the same cell size and threshold of the ones shown in Figure 4) and measured the slope k of the corresponding $I_{\mathrm{Rad}}-I_{\mathrm{H}\alpha}$ correlation. Then, by bootstrapping a value of k from the best-fit of each cycle, we composed a distribution of 100 slopes for each galaxy. In Figure 7 we report the final distributions and the mean and standard deviation of the slope k for each galaxy. The values reported in Figure 4 fall within these distributions. This supports that the results presented in Section 3 are not biased by the choice of the grids.
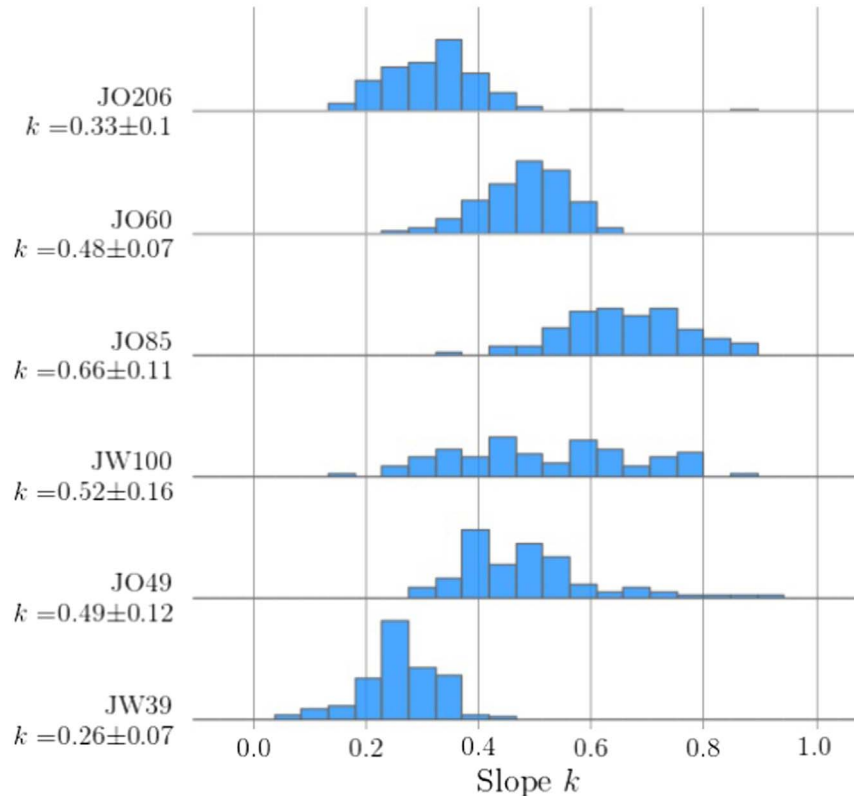
Figure 7. Results of MCptp with 100 iterations for each galaxy of the GASP-LOFAR sample. For each galaxy, the mean and the standard deviation of the distribution is reported in the respective label.

ORCID iDs

Alessandro Ignesti ⬧ https://orcid.org/0000-0003-1581-0092
Benedetta Vulcani ⬧ https://orcid.org/0000-0003-0980-1499
Bianca M. Poggianti ⬧ https://orcid.org/0000-0001-8751-8360
Alessia Moretti ⬧ https://orcid.org/0000-0002-1688-482X
Timothy Shimwell ⬧ https://orcid.org/0000-0001-5648-9069
Andrea Botteon ⬧ https://orcid.org/0000-0002-9325-1567
Reinout J. van Weeren ⬧ https://orcid.org/0000-0002-0587-1660
Ian D. Roberts ⬧ https://orcid.org/0000-0002-0692-0911
Jacopo Fritz ⬧ https://orcid.org/0000-0002-7042-1965
Neven Tomičić ⬧ https://orcid.org/0000-0002-8238-9210
Giorgia Peluso ⬧ https://orcid.org/0000-0001-5766-7154
Rosita Paladino ⬧ https://orcid.org/0000-0001-9143-6026
Myriam Gitti ⬧ https://orcid.org/0000-0002-0843-3009
Ancla Müller ⬧ https://orcid.org/0000-0001-9184-7845
Sean McGee ⬧ https://orcid.org/0000-0003-3255-3139
Marco Gullieuszik ⬧ https://orcid.org/0000-0002-7296-9780

References

Akritas, M. G., & Bershady, M. A. 1996, ApJ, 470, 706
Astropy Collaboration, Price-Whelan, A. M., Sipőcz, B. M., et al. 2018, AJ, 156, 123
Astropy Collaboration, Robitaille, T. P., Tollerud, E. J., et al. 2013, A&A, 558, A33
Baldwin, J. A., Phillips, M. M., & Terlevich, R. 1981, PASP, 93, 5
Basu, A., Beck, R., Schmidt, P., & Roy, S. 2015, MNRAS, 449, 3879
Beck, R., & Krause, M. 2005, AN, 326, 414
Bellhouse, C., McGee, S. L., Smith, R., et al. 2021, MNRAS, 500, 1285
Berlok, T., & Pfrommer, C. 2019, MNRAS, 489, 3368
Bertocco, S., Goz, D., Tornatore, L., et al. 2020, in ASP Conf. Ser., 527, Astronomical Data Analysis Software and Systems XXIX, ed. R. Pizzo et al. (San Francisco, CA: ASP), 303
Boselli, A., Fossati, M., & Sun, M. 2022, A&ARv, 30, 3
Boselli, A., & Gavazzi, G. 2006, PASP, 118, 517
Briggs, D. S. 1995, AAS Meeting, 187, 112.02
Cardelli, J. A., Clayton, G. C., & Mathis, J. S. 1989, ApJ, 345, 245
Carilli, C. L., & Taylor, G. B. 2002, ARA&A, 40, 319
Chabrier, G. 2003, PASP, 115, 763
Chen, H., Sun, M., Yagi, M., et al. 2020, MNRAS, 496, 4654
Cleland, C., & McGee, S. L. 2021, MNRAS, 500, 590
Condon, J. J. 1992, ARA&A, 30, 575
Condon, J. J., Cotton, W. D., Greisen, E. W., et al. 1998, AJ, 115, 1693
Cottle, J., Scannapieco, E., Brüggen, M., Banda-Barragán, W., & Federrath, C. 2020, ApJ, 892, 59
de Gasperin, F., Dijkema, T. J., Drabent, A., et al. 2019, A&A, 622, A5
de Gasperin, F., Williams, W. L., Best, P., et al. 2021, A&A, 648, A104
Dursi, L. J., & Pfrommer, C. 2008, ApJ, 677, 993
Eales, S., Dunne, L., Clements, D., et al. 2010, PASP, 122, 499
Ebeling, H., Ma, C.-J., & Barrett, E. 2014, ApJS, 211, 21
Farber, R. J., Ruszkowski, M., Tonnesen, S., & Holguin, F. 2022, MNRAS, 512, 5927
Fossati, M., Fumagalli, M., Boselli, A., et al. 2016, MNRAS, 455, 2028
Fritz, J., Moretti, A., Gullieuszik, M., et al. 2017, ApJ, 848, 132
Fumagalli, M., Fossati, M., Hau, G. K. T., et al. 2014, MNRAS, 445, 4335
Gavazzi, G. 1978, A&A, 69, 355
Gavazzi, G., & Boselli, A. 1999, A&A, 343, 93
Gavazzi, G., Contursi, A., Carrasco, L., et al. 1995, A&A, 304, 325
Gavazzi, G., & Jaffe, W. 1986, ApJ, 310, 53
Ge, C., Luo, R., Sun, M., et al. 2021, MNRAS, 505, 4702
Gullieuszik, M., Poggianti, B. M., McGee, S. L., et al. 2020, ApJ, 899, 13
Gürkan, G., Hardcastle, M. J., Smith, D. J. B., et al. 2018, MNRAS, 475, 3010
Heesen, V. 2021, Ap&SS, 366, 117
Heesen, V., Dettmar, R.-J., Krause, M., Beck, R., & Stein, Y. 2016, MNRAS, 458, 332
Heesen, V., Buie, E. I., Huff, C. J., et al. 2019, A&A, 622, A8

Heesen, V., Staffehl, M., Basu, A., et al. 2022, A&A, 664, A83
Hoernes, P., Berkhuijsen, E. M., & Xu, C. 1998, A&A, 334, 57
Ignesti, A. 2022, NewA, 92, 101732
Ignesti, A., Shimwell, T., Brunetti, G., et al. 2020, A&A, 643, A172
Ignesti, A., Vulcani, B., Poggianti, B. M., et al. 2022, ApJ, 924, 64
Kennicutt, R. C., & Evans, N. J. 2012, ARA&A, 50, 531
Kennicutt, R. C., Jr. 1998, ARA&A, 36, 189
Kozieł-Wierzbowska, D., Vale Asari, N., Stasińska, G., et al. 2017, ApJ, 846, 42
Lacki, B. C. 2013, MNRAS, 431, 3003
Lacki, B. C., & Thompson, T. A. 2010, ApJ, 717, 196
Longair, M. S. 2011, High Energy Astrophysics (Cambridge: Cambridge Univ. Press)
Luber, N., Müller, A., van Gorkom, J. H., et al. 2022, ApJ, 927, 39
Moretti, A., Paladino, R., Poggianti, B. M., et al. 2020, ApJ, 889, 9
Müller, A., Poggianti, B. M., Pfrommer, C., et al. 2021, NatAS, 5, 159
Murphy, E. J. 2009, ApJ, 706, 482
Murphy, E. J., Kenney, J. D. P., Helou, G., Chung, A., & Howell, J. H. 2009, ApJ, 694, 1435
Niklas, S., Klein, U., & Wielebinski, R. 1995, A&A, 293, 56
Offringa, A. R., McKinley, B., Hurley-Walker, N., et al. 2014, MNRAS, 444, 606
Pacholczyk, A. G. 1970, in Radio Astrophysics: Nonthermal Processes in Galactic and Extragalactic Source, ed. A. G. Pacholczyk (San Francisco, CA: W. H. Freeman & Co.)
Panessa, F., Baldi, R. D., Laor, A., et al. 2019, NatAS, 3, 387
Peluso, G., Vulcani, B., Poggianti, B. M., et al. 2022, ApJ, 927, 130
Pfrommer, C., & Dursi, L. J. 2010, NatPh, 6, 520
Poggianti, B. M., Moretti, A., Gullieuszik, M., et al. 2017a, ApJ, 844, 48
Poggianti, B. M., Jaffé, Y. L., Moretti, A., et al. 2017b, Natur, 548, 304
Poggianti, B. M., Ignesti, A., Gitti, M., et al. 2019a, ApJ, 887, 155
Poggianti, B. M., Gullieuszik, M., Tonnesen, S., et al. 2019b, MNRAS, 482, 4466
Radovich, M., Poggianti, B., Jaffé, Y. L., et al. 2019, MNRAS, 486, 486
Ramos-Martínez, M., Gómez, G. C., & Pérez-Villegas, Á. 2018, MNRAS, 476, 3781
Roberts, I. D., van Weeren, R. J., McGee, S. L., et al. 2021a, A&A, 652, A153
Roberts, I. D., van Weeren, R. J., McGee, S. L., et al. 2021b, A&A, 650, A111
Roberts, I. D., van Weeren, R. J., Timmerman, R., et al. 2022, A&A, 658, A44
Robitaille, T., & Bressert, E. 2012, APLpy: Astronomical Plotting Library in Python, Astrophysics Source Code Library, ascl:1208017
Ruszkowski, M., Brüggen, M., Lee, D., & Shin, M. S. 2014, ApJ, 784, 75
Schlafly, E. F., & Finkbeiner, D. P. 2011, ApJ, 737, 103
Shimwell, T. W., Röttgering, H. J. A., Best, P. N., et al. 2017, A&A, 598, A104
Shimwell, T. W., Tasse, C., Hardcastle, M. J., et al. 2019, A&A, 622, A1
Shimwell, T. W., Hardcastle, M. J., Tasse, C., et al. 2022, A&A, 659, A1
Smirnov, O. M., & Tasse, C. 2015, MNRAS, 449, 2668
Smith, R. J., Lucey, J. R., Hammer, D., et al. 2010, MNRAS, 408, 1417
Sparre, M., Pfrommer, C., & Ehlert, K. 2020, MNRAS, 499, 4261
Strong, A. W., Moskalenko, I. V., & Ptuskin, V. S. 2007, ARNPS, 57, 285
Tabatabaei, F. S., Martinsson, T. P. K., Knapen, J. H., et al. 2016, ApJL, 818, L10
Tabatabaei, F. S., Schinnerer, E., Murphy, E. J., et al. 2013, A&A, 552, A19
Tabatabaei, F. S., Schinnerer, E., Krause, M., et al. 2017, ApJ, 836, 185
Taffoni, G., Becciani, U., Garilli, B., et al. 2020, in ASP Conf. Ser., 527, Astronomical Data Analysis Software and Systems XXIX, ed. R. Pizzo et al. (San Francisco, CA: ASP), 307
Tasse, C. 2014, A&A, 566, A127
Tasse, C., Hugo, B., Mirmont, M., et al. 2018, A&A, 611, A87
Tasse, C., Shimwell, T., Hardcastle, M. J., et al. 2021, A&A, 648, A1
Tonnesen, S., & Bryan, G. L. 2021, ApJ, 911, 68
Tonnesen, S., & Stone, J. 2014, ApJ, 795, 148
van Haarlem, M. P., Wise, M. W., Gunst, A. W., et al. 2013, A&A, 556, A2
van Weeren, R. J., Williams, W. L., Hardcastle, M. J., et al. 2016, ApJS, 223, 2
van Weeren, R. J., Shimwell, T. W., Botteon, A., et al. 2021, A&A, 651, A115
Vollmer, B., Beck, R., Kenney, J. D. P., & van Gorkom, J. H. 2004, AJ, 127, 3375
Vollmer, B., Soida, M., Beck, R., et al. 2013, A&A, 553, A116
Vollmer, B., Soida, M., Chung, A., et al. 2010, A&A, 512, A36
Vulcani, B., Poggianti, B. M., Gullieuszik, M., et al. 2018, ApJL, 866, L25
White, S. V., Jarvis, M. J., Kalfountzou, E., et al. 2017, MNRAS, 468, 217
Williams, W. L., van Weeren, R. J., Röttgering, H. J. A., et al. 2016, MNRAS, 460, 2385